

# Alkaline Earth versus Noble Metal Particles on MgO Thin Films: Growth and Optical Properties

Philipp Myrach, Niklas Nilus,\* and Hans-Joachim Freund

Fritz-Haber Institut der Max-Planck Gesellschaft, Department of Chemical Physics, Faradayweg 4-6, D-14195 Berlin, Germany

Received: May 5, 2009; Revised Manuscript Received: June 12, 2009

Nucleation and growth of Mg, Ca, and Au particles on 8 ML thick MgO/Mo(001) films have been investigated by scanning tunneling microscopy (STM). Whereas the alkaline earth metals strongly interact with the MgO surface and form islands that are in registry with the square oxide lattice, a reduced coupling is suggested for Au on the basis of the observed hexagonal particle shapes. Optical properties of the metal particles are probed by injecting electrons from the STM tip into individual deposits and detecting the resulting photon emission. The overall spectral shape is governed by a plasmon-mediated photon emission that is characteristic for the different particle materials. However, a distinct fine-structure that is superimposed on the plasmon response is found to be independent of the chemical identity and geometry of the particles. This spectral contribution is assigned to the discrete excitation behavior of particle plasmons via inelastic electron transport through the double-barrier STM junction.

## 1. Introduction

Noble metal particles, especially of silver and gold, in dielectric matrices have been intensively investigated for almost a hundred years because of their unique optical properties.<sup>1</sup> For particle sizes below the wavelength of light, sharp and intense peaks appear in the emission and absorption spectra, which originate from collective excitations in the particle electron gas and are commonly referred to as Mie plasmons. As the energy position of such plasmon modes can be shifted over the entire UV–vis spectrum, noble metal particles are widely used in technological applications, for instance in optical filters, photon wave guides, stained glass, and as active components in photocatalytic and electro–optical devices.<sup>1,2</sup>

The occurrence of strong plasmon excitations is closely connected to the presence of a highly polarizable electron gas, whose fundamental modes should not interfere with single-electron excitations such as d-band transitions. This premise is perfectly fulfilled for Ag 5s and Au 6s electrons in noble metal particles that are energetically well-separated from the respective d-bands being far below the Fermi level.<sup>1</sup> However, suitable conditions for plasmon excitations are also present in most alkali and earth alkali metals, making them promising candidates for optical applications as well.<sup>3–5</sup> The reason why simple metal clusters are much less investigated than their noble metal counterparts lies in their notorious chemical instability in the presence of oxygen and water.

Despite certain similarities with noble metals, simple metal particles exhibit a number of differences in their optical response due to the absence of d-electrons. The spatially localized d-states usually introduce a strong depolarization field in the cluster volume that inhibits the oscillations of the s-like electron gas.<sup>6</sup> As a consequence, the plasmon energy  $\hbar\omega_p$  in Ag and Au particles is considerably lower than that in most simple metal aggregates and does not follow the simple square root dependence on the electron density  $n$  as observed for ideal plasmas:  $\hbar\omega_p = [(ne^2)/(\epsilon_0 m)]^{1/2}$  ( $m$ , electron mass;  $e$ , elementary charge).<sup>7</sup>

In contrast, this relationship is fulfilled with good accuracy for most alkali metals. Additionally, the plasmon energy shows an opposite particle size dependence for simple and noble metals.<sup>1,6</sup> In the first case,  $\hbar\omega_p$  shifts to lower values for decreasing particle sizes due to the enhanced effect of electron spill-out and the concomitant reduction of electron density.<sup>8,9</sup> For Ag and Au, on the other hand, the diminishing influence of the d-depolarization field induces a blue shift of  $\hbar\omega_p$  with decreasing size.<sup>10,11</sup> Deviations in the optical characteristic can finally be expected from the different growth behaviors of simple versus noble metals on dielectric surfaces. As a result of their enhanced reactivity, simple metals often aggregate in the form of flat islands, whereas noble metals tend to form three-dimensional particles with large height to diameter ratios.

Despite their distinct optical properties, experiments on simple metal particles are still scarce, whereas an overwhelming number of studies have been performed for Ag and Au.<sup>1</sup> To counteract this trend, this paper deals with the optical properties of Mg and Ca deposits on atomically flat MgO films. To enable comparison with noble metal aggregates, we performed complementary studies with Au on the same support. In all three cases, optical experiments are carried out on the single cluster level, using the tunnel current of a scanning tunneling microscope (STM) to stimulate plasmon excitations.<sup>11,12</sup> The resulting photon emission is detected in a wavelength-sensitive scheme and directly linked to the structure of the emitting entity as revealed from topographic STM images. The approach is therefore ideally suited to correlate the geometric and optical properties of single metal particles within one spatially resolved experiment.<sup>11,13</sup>

## 2. Experimental Section

Measurements are carried out with a liquid nitrogen-cooled (100 K) STM operated in ultrahigh vacuum. The microscope is optimized to detect photon emission from the tip–sample junction during tunneling. For this purpose, a Beetle-type STM head is surrounded by a parabolic mirror, which collects light from the gap region and guides it to a grating spectrograph/

\* Corresponding author: nilus@fhi-berlin.mpg.de.

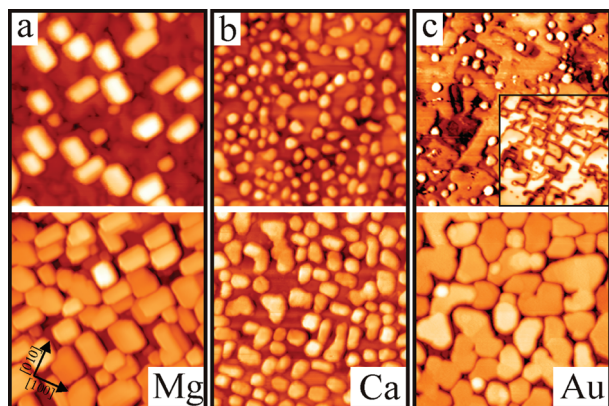


**Figure 1.** STM topographic images of Mg, Ca, and Au particles on 8 ML MgO/Mo(001) ( $75 \times 75 \text{ nm}^2$ ,  $U_s = 4.5 \text{ V}$ , and  $I = 30 \text{ pA}$ ). Images in the upper (lower) row are for the following nominal metal exposures: Mg, 2 (5) ML; Ca, 1 (3) ML; and Au, 0.5 (5) ML. Inset in the upper right image shows the bare MgO surface with the [100]-oriented dislocations visible as dark lines.

CCD detector unit situated outside the vacuum chamber. The large acceptance angle for photon collection and high sensitivity of the optical system enables analysis of photon yields as small as 10 photons per second in the wavelength window of 200–1200 nm.<sup>14</sup> Thin MgO films grown on sputtered and annealed Mo(001) crystals are used as support for the particles. The films are prepared by Mg deposition in an  $\text{O}_2$  ambience of  $1 \times 10^{-7}$  mbar at room temperature, followed by sample annealing in vacuum to 1100 K. The nominal film thickness is adjusted to 7–8 layers on the basis of distinct cross-like reflexes that emerge in this thickness regime in low-energy electron reflection (LEED).<sup>15</sup> The elongation of the LEED spots along the orthogonal [110] directions reflects the pronounced mosaicity of the oxide film. The formation of mosaics is closely related to the compensation of oxide strain induced by the 5% lattice mismatch with the Mo support.<sup>16</sup> A complete discussion of the strain relaxation in the MgO/Mo(001) system as a function of film thickness is presented in ref 17. The Mg, Ca, and Au particles are prepared by physical vapor deposition onto freshly prepared MgO films at room temperature. The nominal coverage is varied between 1 and 10 ML as calibrated by deposition experiments on the bare Mo(001) surface, where layer-by-layer growth enables direct coverage determination via STM imaging.

### 3. Results and Discussion

**3.1. Morphology of Metal Particles.** Figure 1 shows STM topographic images of Mg, Ca, and Au particles on MgO/Mo(001) for two different metal exposures. In all three cases, the metal nucleates at step-like dislocation lines oriented along the nonpolar MgO[100] directions (Figure 1c inset). These line defects are in fact the boundaries of the oxide mosaics and are usually pinned by screw dislocations at the metal–oxide interface.<sup>15,17</sup> They represent not only topographic defects but also exhibit a different electronic structure and a 1.0–1.5 eV higher work function than the defect-free oxide patches, indicating an oxygen-rich defect stoichiometry.<sup>18</sup> Those structural and electronic peculiarities are the likely origin for a preferred nucleation of metal atoms along the line defects. In contrast, particle formation on regular oxide terraces is rarely observed, and point defects seem to play a minor role for the nucleation.<sup>19,20</sup>

Deposition of all three metals onto the MgO film results in the formation of faceted nanoparticles, indicating their crystalline

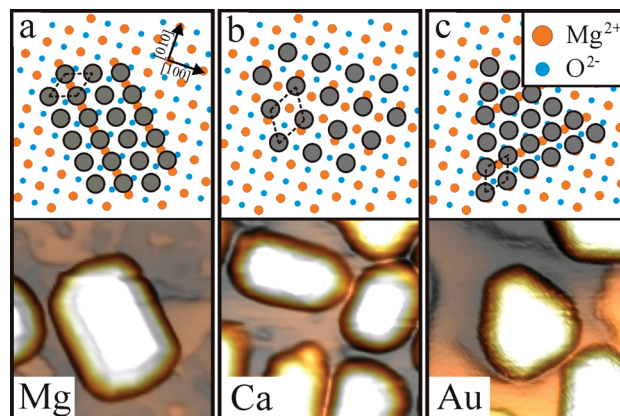


**Figure 2.** Structure model of the particle–oxide interface and corresponding close-up STM image of (a) individual Mg, (b) Ca, and (c) Au particles on MgO/Mo(001) ( $10 \times 10 \text{ nm}^2$ ,  $U_s = 4.5 \text{ V}$ , and  $I = 30 \text{ pA}$ ). Dashed lines mark unit cells of the Mg, Ca, and Au(111) surfaces, respectively.

nature. Mg deposits develop characteristic rectangular shapes with the long axes running along the MgO[110] or [1 $\bar{1}$ 0] direction (Figure 1a).<sup>21</sup> The particle edges are thus parallel to the polar MgO lattice directions and follow either the oxygen or magnesium rows. The top facets are atomically flat, and single Mg step edges are frequently resolved in the STM. With increasing coverage, the particles preferentially grow in height, and their aspect (height to width) ratio gradually approaches one. Simultaneously, the particle top facets develop distinct 120° angles, indicating a hexagonal symmetry of the underlying lattice, although the overall particle shape remains rectangular (Figure 2a). Above 5 ML nominal coverage, coalescence of adjacent particles sets in and a rough Mg film develops on the surface. Also, Ca particles grow predominantly with rectangular or square-like shapes (Figure 1b). The edge directions are, however, tilted by 45° with respect to the Mg case and thus align with the nonpolar MgO[100]-directions. With increasing Ca exposure, the 2-fold cluster symmetry gradually converts to hexagonal shapes, suggesting a diminishing template effect of the oxide support. Simultaneously, the clusters become hemispherical, and their initially flat top facets vanish. Ca deposits are characterized by a smaller aspect ratio of  $\sim 0.6$  and a higher number density on the surface ( $n_{\text{Ca}} = 25 \times 10^{11} \text{ cm}^{-2}$  versus  $n_{\text{Mg}} = 6.8 \times 10^{11} \text{ cm}^{-2}$ ). In contrast to Ca and Mg, Au particles do not reflect the 4-fold symmetry of the MgO support and develop triangular and hexagonal shapes already in the initial growth stage (Figure 1c).<sup>20</sup> Nonetheless, the particle orientation is not arbitrary, as one of its main axes always follows the [110] or [1 $\bar{1}$ 0] direction of MgO(001). Au clusters have the lowest aspect ratio (0.3) of all three investigated metals and adapt an intermediate number density of approximately  $12 \times 10^{11} \text{ cm}^{-2}$ .

On the basis of the distinct particle shapes observed in the STM, structure models can be established for the particle–oxide interface in all three cases. The alignment of the Mg particle edges with the MgO[110] direction indicates that interfacial Mg atoms bind to oxygen rows in the surface, resuming the stacking sequence of rock salt MgO (Figure 2a). The formation of atomically flat and hexagonal top facets, however, suggests a [111] growth direction of the Mg deposits that would also be in line with the low surface free energy of this particular Mg plane. A pseudohexagonal Mg layer can indeed be realized on MgO(001), assuming that the Mg adsorption sites alternate from top to bridge positions on adjacent oxygen rows (Figure 2a). In this configuration, any unfavorable Mg adsorption atop the oxide

Mg<sup>2+</sup> ions is avoided and binding takes place exclusively to O<sup>2-</sup> top and bridge sites. Because of the mismatch between the Mg and MgO lattice constants (4.52 versus 4.21 Å), the Mg islands experience a compressive strain of -4.5% along the close-packed O rows that increases to -8% in the perpendicular direction. This strain difference in both growth directions is responsible for the pronounced rectangular island shapes. The particles grow preferentially along those O rows, where Mg binds in the on-top or bridge positions, whereas in the perpendicular direction, the growth is strongly inhibited by the high deformation energy. The formation of rectangular Mg particles with two orthogonal orientations finally reflects the 4-fold symmetry of the MgO surface (Figure 1a).

A similar model is revealed for the Ca-MgO interface with the only difference being that the island orientation follows the mixed Mg-O rows along the [100] direction. The deviating orientation with respect to Mg is easily explained by the larger Ca lattice parameter of 5.59 Å. The Ca nearest neighbor distance now matches the O-Mg-O unit length along the [100] direction by +5.8%. Assuming again the formation of Ca(111) planes, a superstructure is proposed where 30% of the Ca atoms bind in the O top positions along the [100]-oriented oxide rows and 60% in the Mg-O bridge sites (Figure 2b). Although the overall deformation energy is smaller than that for the Mg-MgO interface, the structure is presumably less favorable because of the small portion of Ca atoms bound to favorable O top sites.<sup>22</sup> The reduced Ca-MgO lattice match is also responsible for the broader shape distribution and absence of flat top facets for the Ca particles (Figure 1b). Still, a certain template effect of MgO(001) becomes manifest in the 2-fold symmetry of the Ca islands. It should be noticed at this point that also the formation of (001)-oriented Ca particles is conceivable, whereby each Ca atom would bind to a surface O<sup>2-</sup> site (mismatch +5.8%). This growth characteristic is, however, disregarded because of the frequent observation of hexagonal Ca islands in the experiment (Figure 1b).

The Au particles adapt hexagonal shapes already in the initial growth stage, suggesting the formation of (111)-oriented Au planes. As a consequence, only one of the three Au lattice directions can be in registry with the square oxide lattice. Along the MgO[110] direction, Au atoms are able to occupy energetically favorable O<sup>2-</sup> sites with only +3% tensile strain (Figure 2c). Already this unidirectional Au-O interaction that does not extend into the orthogonal direction seems to be sufficient to fix the orientation of the Au particles on the MgO surface. The low aspect ratio of Au particles on thin MgO films has already been observed in earlier studies and was traced back to an unusually high Au adhesion to the thin oxide film.<sup>23</sup> The strong Au-MgO interaction hereby results from the possibility to charge or polarize the Au islands in the presence of the Mo support underneath, which in turn enables new electrostatic and polaronic interaction schemes with the oxide surface.<sup>24</sup> In the limit of ultrathin layers (1-3 ML), Au even resumes a two-dimensional growth mode,<sup>23</sup> which evolves into the formation of flat particles on 7-8 ML thick films.<sup>20</sup>

In summary, the distinct shapes of Mg, Ca, and Au particles on the MgO film result from the lattice mismatch between particles and oxide support as well as from the different metal affinities to bind to anionic sites in the MgO layer. The observed binding trends are in part corroborated by recent DFT calculations,<sup>22,24-26</sup> which clearly demonstrate the strong preference of Au and Ca to bind to O<sup>2-</sup> sites in the MgO surface. Cationic sites are exclusively occupied by negatively charged Au ions on monolayer oxide films, which were not explored in

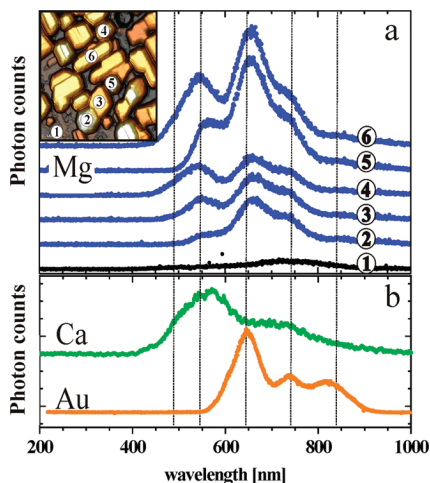
this study.<sup>24</sup> For Ca on MgO(001) in particular, the binding energy was found to increase dramatically at step edges and kink sites, where the Ca is able to interact with two or three oxygen ions, respectively. The presence of Mg vacancies or extra O atoms at the step edge further enlarges the Ca binding strength. The latter finding is in agreement with the observed nucleation of the alkaline earth metals to the presumably oxygen-rich dislocation lines.<sup>18</sup> According to the DFT results, the Ca develops (001)-oriented islands at higher coverage, which is in contrast to the hexagonal particle shapes observed here and the deduced structure model based on (111)-oriented Ca deposits. In many details, Mg is expected to show a similar binding behavior to MgO(001) as derived for the Ca case.

In addition to the binding preference to surface O<sup>2-</sup> ions, the lattice match between the ad-metal and the MgO film influences the particle shapes. A favorable registry between MgO and Mg(111) enables the formation of quasi-rectangular Mg particles. Although the lattice match is worse for Ca, the interfacial Ca-O interaction remains sufficiently strong to impress the 4-fold MgO symmetry onto the Ca particles as well. Only in the case of gold do hexagonal particles develop on the square MgO lattice right from the beginning.

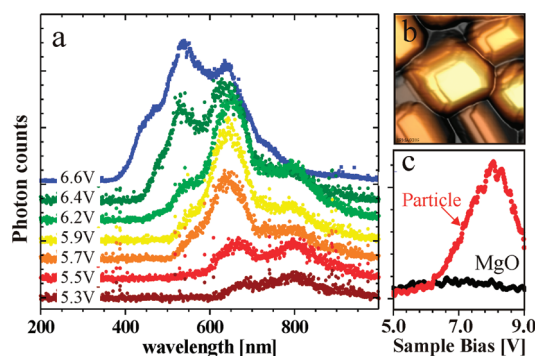
**3.2. Optical Properties of Metal Particles.** The optical characteristic of Mg, Ca, and Au particles is probed by injecting electrons with 5.0-12.0 eV from the STM tip into individual deposits and analyzing the emitted UV-vis radiation.<sup>11,13</sup> The high spatial localization of the electron beam of ~1 nm diameter ensures the excitation of a single particle in this case. Emission spectra with good signal-to-noise ratio are acquired for tunnel currents of 2-3 nA and photon accumulation times of 3-5 min. The structural integrity of the surface is verified by taking STM images before and after each spectral run. To benefit from the electromagnetic field enhancement in the tip-sample cavity and to maximize the emission yield, we used Ag tips with strong optical near-fields in the experiments.<sup>12</sup> The photon response of the pristine MgO film is governed by an emission line at ~700 nm, which is assigned to radiative electron transitions between field emission resonances in the tip-sample gap.<sup>18</sup> Exciton-mediated light emission shows up only for excitation energies above 30 eV, when an intense emission peak becomes visible at 400 nm.<sup>15,18</sup> After metal deposition, the optical signal from the pristine MgO film is swamped by photons from the ad-particles.

Figure 3a displays photon emission spectra of differently sized Mg particles taken with 7.5 V excitation bias, together with an STM image of the probed species. All spectra are characterized by a set of emission peaks (marked by vertical lines), appearing at similar energies but with varying intensities for the different particles. In a spectral series taken as a function of the excitation bias, the emission starts around 5.5 V with a low-energy peak at 820 nm (1.5 eV) (Figure 4a). With increasing bias, additional peaks become visible with maximum positions located at ~640 (1.95), ~540 (2.3), and ~490 nm (2.5 eV), whereby the peaks at 640 and 540 nm exhibit the highest intensity. Furthermore, the total emitted intensity, as detected by a photomultiplier tube, first rises with excitation bias but starts decreasing again above 8.0 V (Figure 4c). Common to all Mg spectra obtained in this study is a sharp cutoff in the photon intensity at 390 nm (3.2 eV).

A similar optical response is observed for Ca and Au particles on the MgO film, as demonstrated by two representative single-particle spectra in Figure 3b. For both metals, the emission comprises again a number of photon peaks that are differently developed in particles of different size and shape. Whereas the



**Figure 3.** (a) Light emission spectra of single Mg particles on 8 ML MgO/Mo(001). Spectra are taken with  $U_s = 7.5$  V,  $I = 2$  nA, and 3 min acquisition time. Vertical lines mark characteristic emission peaks. Probed particles are shown in the inset ( $100 \times 100$  nm<sup>2</sup>, 5.2 V). (b) Light emission spectra of a single Ca and Au particle taken at similar conditions as in panel a.



**Figure 4.** (a) Light emission spectra taken as a function of excitation bias for the single Mg particle shown in panel b ( $I = 2$  nA, acquisition time 3 min). With increasing bias voltage, new blue-shifted emission lines emerge in the spectra until a cutoff is reached at 390 nm. (c) Emission intensity versus sample bias as measured with a photomultiplier tube for a Mg particle and bare oxide film.

emission maximum for Ca is typically observed at 540 nm (2.3 eV), it shifts to 650 nm (1.9 eV) for Au particles on the MgO film. Also, the emission onset differs in a characteristic manner, changing from 400 nm (3.1 eV) for Ca to 510 nm (2.4 eV) for Au particles, respectively. Besides the deviations in the overall spectral shape, a set of low-energy emission peaks remains distinguishable also in the spectra of Ca and Au particles. Surprisingly, these subpeaks appear at similar energy positions as for Mg and seem thus to be independent of the cluster material and the actual tip state. They are even preserved in spectral averages, produced from adding together more than 100 single-particle spectra of the different metals (Figure 5a). This finding suggests that the emission signature of Mg, Ca, and Au particles on MgO thin films combines two contributions: an element-specific one that is responsible for emission onset and maximum position and a material independent one that governs the spectral fine-structure.

Several mechanisms are conceivable to explain the observed photon emission. In each scenario, plasmon excitations in the particle electron gas will be of pivotal importance because of their efficient coupling to light and their high oscillator strengths. Nanoparticles of all three metals support Mie plasmons<sup>1</sup> as a result of their s-dominated state density at the Fermi level. An

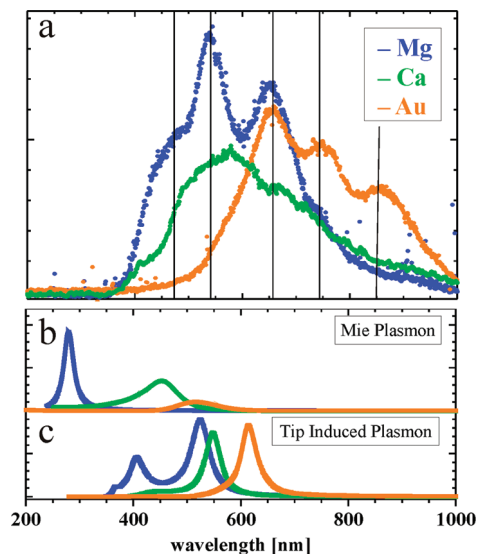


**Figure 5.** (a) Emission characteristics of Mg, Ca, and Au particles obtained from averaging more than 100 single-particle spectra taken in different experimental runs. Calculated emission behavior of (b) Mie plasmons in Mg, Ca, and Au particles with the experimental aspect ratio and (c) tip-induced plasmons for Mg–Ag, Ca–Ag, and Au–Ag tunnel junctions.

estimation of the plasmon energy is obtained from calculating the energy-dependent polarizability  $\alpha(\omega)$  of a metal spheroid in a dielectric matrix<sup>1</sup>

$$\alpha_{(1,0)}(\omega) \propto \frac{\varepsilon(\omega) - \varepsilon_m}{3\varepsilon_m + 3L_{\perp}[\varepsilon(\omega) - \varepsilon_m]} \quad (1)$$

Hereby,  $\varepsilon(\omega)$  is the experimentally determined dielectric function of the particle material, and  $\varepsilon_m$  is the average dielectric constant of the surrounding medium consisting of 30% MgO ( $\varepsilon_r = 3.2$ ) and 70% vacuum.<sup>27</sup> The particle shape as determined from experimental aspect ratios is introduced via the depolarization factor  $L_{\perp}$ . Only plasmon oscillations perpendicular to the sample surface are considered (1,0 plasmon) as mainly this mode is excited by the injected electrons from the STM tip. Already this crude model is able to reproduce the sequence of the observed emission maxima (Figure 5b). The calculated (1,0) Mie mode shifts down in energy when going from Mg (4.5 eV) to Ca (3.2 eV) and Au particles (2.5 eV), reflecting the decreasing electron density in the simple metals as well as the influence of the d-states in gold.

A better quantitative agreement with the experimental data is obtained when the influence of the STM tip is taken into account.<sup>12,28</sup> The presence of a metal tip in nanometer distance from the particle strongly enhances the polarizability of the system, inducing a red shift of the plasmon modes and the emergence of a low-energy emission tail. The underlying physics is captured by the model of tip-induced plasmons developed by Johansson et al.,<sup>29</sup> which relates the field enhancement in the tip–sample cavity to the excitation of coupled plasmon modes in both electrodes. The theoretical description of tip-induced plasmons is restricted to model geometries consisting of a metal sphere above a flat surface and not easily adaptable to the present tip–particle–oxide–support system.<sup>29</sup> Nonetheless, a rough idea of the tip influence can be obtained by reversing the model geometry, taking the flat electrode as the tip and the metal sphere as the nanoparticle. This approach is justified as long as the tip curvature is much larger than that of

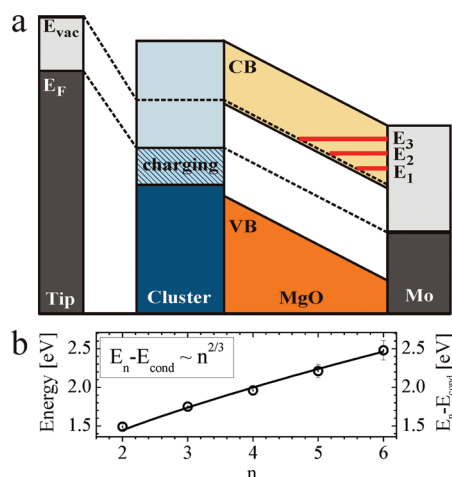


**Figure 6.** (a) Potential diagram of an STM junction consisting of tip, nanoparticle, oxide film, and Mo support. The particle is isolated from the outer electrodes by two tunnel barriers and adjusts its Fermi level according to the applied sample bias (charging). The MgO conduction band (CB) is quantized into Gundlach resonances ( $E_1$ – $E_3$ ), which form above the vacuum level in the electric field between particle and Mo support. Inelastic electron transitions between the Gundlach resonances and MgO conduction band onset provide the energy for the plasmon excitations. (b) Energy of emission peaks observed for single Mg particles (○) fitted to an  $n^{2/3}$  dependence on the quantum number  $n$  of the Gundlach states.

the metal deposits. The corresponding optical response is plotted for an Ag tip–particle junction in Figure 5c. In accordance with the expected tip effect, all plasmon peaks experience a shift to lower energies, whereby the Mg plasmon additionally splits because of interference with the tip modes. The experimental trends, especially the onset and peak wavelength of the emitted light, are well-reproduced for the three particle types. Only the calculated line widths are substantially smaller than the experimental ones, most likely because the highly dissipative Mo support was neglected in the calculations.

Apparently, the model of tip-mediated plasmon excitations is able to describe the spectral envelope of the particle emission but fails to explain the observed fine-structure in the spectra. For all three metals, up to five sub-bands are resolved, whose energy positions are approximately independent of the chemical nature and size of the ad-particles (Figure 5a). A possible interpretation in terms of in-plane or higher-order plasmons can thus be discarded because those modes should strongly depend on the particle identity. In fact, the observed “universality” of the detected peaks suggests a participation of the MgO/Mo thin film, being the constant structural element in all experiments. To account for a possible influence of the thin film support, the excitation process of particle plasmons via electron tunneling through the double-barrier STM junction needs to be illuminated (Figure 6).

Plasmon modes in an STM junction are driven by an energy transfer from inelastically tunneling electrons.<sup>12,29</sup> In the present system, electron energy losses take place either in the vacuum gap separating tip and particle or in the oxide spacer layer (Figure 6).<sup>30</sup> An energy transfer to plasmon modes directly inside the particle seems to be unlikely as competing decay channels such as intraband transitions or phonon excitations, are available in the deposit. For the given geometry, the oxide film is the most susceptible region for inelastic losses. Because of its large thickness of  $\sim 15$  Å, tunneling through the MgO is clearly the limiting step for electron transport between tip and sample, while tunneling through the vacuum gap is comparatively easy.

To compensate this difference in the tunneling rates, the metal particle charges in the biased junction, thereby lowering the barrier height associated with the oxide film.<sup>31</sup> When the transmission probability of vacuum and oxide gap are in equilibrium, the potential step across the MgO will be higher or at least comparable with the one across the vacuum, rendering the oxide film the likely place for energy losses (Figure 6). With this mechanism in mind, the fine-structure in the optical spectra can be related to peculiarities of the inelastic electron transport through the MgO film as discussed below.

Plasmon excitations in Mg, Ca, and Au particles require a sample bias of more than 5.5 V (Figure 4), which is substantially higher than the MgO/Mo work function  $\phi_s$  of 3.3–3.9 eV.<sup>22,32</sup> In this bias regime, the current flow is not governed by tunneling through the MgO band gap but involves quantized energy levels  $E_n$  in the oxide conduction band, so-called Gundlach resonances.<sup>33,34</sup> These resonances can be regarded as vacuum states that form in the oxide region confined by the Mo surface on one side and the vacuum energy  $E_{vac}$  on the other. The slope of the vacuum energy is hereby determined by the electric field  $F$  between the charged particle and Mo support and amounts to some tenths V/Å (Figure 6). The existence of energetically confined transport channels implies that energy losses of tunneling electrons should also obey a certain discretization. Possible loss energies  $E_{loss}$  are hereby given by the difference between a Gundlach resonance  $E_n$  ( $1 < n < 5$ ) and the MgO conduction band onset  $E_{cond}$ , being the lowest final state for an inelastic transition. Treating the Gundlach resonances as eigenstates in a triangular potential, given by the electric field  $F$  and the work function  $\phi_s$ , enables us to estimate the loss energies<sup>35</sup>

$$E_{loss} = E_n - E_{cond} = \phi_s - E_{cond} + \left( \frac{3\pi\hbar eF}{2\epsilon_{MgO}\sqrt{2m}} \right)^{2/3} n^{2/3} \quad (2)$$

In principle, only for the loss energies given by eq 2, an excitation of plasmon modes should be probable in the tip–sample cavity, although this discrete behavior will be considerably broadened by the inhomogeneous surface morphology. The observed optical response is thus assigned to a plasmon-mediated emission channel that is active in a broad energy window, convolved with the discrete excitation function due to inelastic electron transport through the Gundlach states. This interpretation explains a number of experimental observations: (i) The fine-structure in the photon emission is found to be independent of the particle material and shape, although plasmon energies are known to be rather sensitive to these parameters. (ii) The energy of fine-structure peaks can be fitted to an  $n^{2/3}$  dependence on the peak number  $n$  (Figure 6b), in accordance to the suggested excitation mechanism (eq 2). The two fit parameters,  $\phi_s - E_{cond} = 0.71$  eV and  $F = 0.4$  V/Å are reasonable. The first value is consistent with the difference between the reported MgO/Mo work function (3.3 to 3.9 eV)<sup>22,32</sup> and the conduction band onset in 8 ML thick MgO films (3.1 eV).<sup>18</sup> The electric field strength, on the other hand, is compatible with a voltage drop of 6 V across the 15 Å thick oxide film, using a simple plate capacitor model. This estimation suggests that at typical excitation conditions of the plasmon-mediated light emission ( $U_s = 7.5$  V), almost 80% of the potential drops in the oxide barrier. (iii) The model explains the high excitation voltage of more than 5.5 V that is required to stimulate the particle emission. Only above this bias value do Gundlach resonances become populated as the initial states for inelastic

electron transport. With increasing sample bias, higher resonances and hence larger loss energies are available, explaining the occurrence of new emission peaks in the optical spectra (Figure 4).

The interplay between a discrete excitation mask and the broad window for plasmon-induced field enhancement in the tip-sample gap therefore rationalizes the observed emission behavior of the MgO-supported metal particles. Hereby, the geometric and dielectric properties of the deposits mainly determine the envelope function of the light emission, whereas the spectral fine-structure relates to the discrete transport properties of the double-barrier junction. The ultimate proof for this model would be the observation of a decreasing (increasing) separation between the emission peaks for thicker (thinner) MgO films due to the different quantization conditions in the oxide conduction band.<sup>33</sup> Experiments along this line were not successful. Whereas the tip-sample junction could not be stabilized for MgO films thicker than 8–10 ML, only the most intense emission peak but no fine-structure was detectable for thinner films. The latter finding indicates the inaccessibility of Gundlach resonances in thin oxide films due to their higher energy and the reduced effect of particle charging.

#### 4. Conclusions

The morphology and optical properties of Mg, Ca, and Au particles on MgO/Mo(001) films have been investigated by STM and light emission spectroscopy. For all three metals, dislocation lines in the oxide film are identified as the preferred nucleation sites. The rectangular shapes of Mg and Ca particles are governed by strong interfacial interactions between the alkaline earth metal and the O<sup>2-</sup> ions in the MgO surface. In contrast, Au deposits are hexagonally shaped due to the weaker O–Au interaction and the unfavorable lattice match with the MgO.

The optical response of the nanoparticles is dominated by plasmon excitations, leading to an element-specific onset and a distinct maximum position of the emitted radiation. A characteristic fine-structure is superimposed on the spectra of the different particles. These subpeaks are attributed to the discrete nature of electron-energy losses for exciting particle plasmons in the double-barrier STM junction. Loss energies are hereby given by the energy positions of Gundlach resonances in the MgO conduction band. The emission characteristic can therefore be considered as a convolution between the plasmon-mediated response of the nanoparticles and discrete excitation mask of the tip-sample junction.

**Acknowledgment.** This work has been supported by the COST Action D41.

#### References and Notes

- (1) Kreibitz U.; Vollmer W. *Optical Properties of Metal Clusters*, Springer Series Materials Science; Springer: Berlin, 1995, Vol. 25.
- (2) Watanabe, K.; Menzel, D.; Nilius, N.; Freund, H.-J. *Chem. Rev.* **2006**, *106*, 4301.
- (3) Bréchnignac, C.; Cahuzac, Ph.; Kebaïli, N.; Leygnier, J.; Sarfati, A. *Phys. Rev. Lett.* **1992**, *68*, 3916.
- (4) Kolwas, K.; Demianiuk, S.; Kolwas, M. *J. Chem. Phys.* **1997**, *106*, 8436.
- (5) Beitia, C.; Borensztein, Y.; Barrera, R. G.; Roman-Velazquez, C. E.; Noguez, C. *Physica B* **2000**, *279*, 25.
- (6) Liebsch, A. *Phys. Rev. B* **1993**, *48*, 11317.
- (7) Kittel C. *Introduction to Solid State Physics*; Wiley: New York, 1996.
- (8) Ekardt W., Ed. *Metal Clusters*; Wiley: Chichester, 1999.
- (9) Solov'yov, I. A.; Solov'yov, A. V.; Greiner, W. *J. Phys. B: At. Mol. Opt. Phys.* **2004**, *37*, L137.
- (10) Tiggesbäumker, J.; Köller, L.; Meiwes-Broer, K. H.; Liebsch, A. *Phys. Rev. A* **1993**, *48*, R17490.
- (11) Nilius, N.; Ernst, N.; Freund, H.-J. *Phys. Rev. Lett.*, **2000**, *84*, 3994.
- (12) Berndt, R. *Scanning Probe Microscopy*; Wiesendanger, R., Ed.; Springer Series Nanoscience and Technology; Springer: Berlin, 1998, p 97.
- (13) Bente, W.; Nilius, N.; Ernst, N.; Freund, H.-J. *Phys. Rev. B* **2005**, *72*, 045403.
- (14) Nilius, N.; Körper, A.; Bozdech, G.; Ernst, N.; Freund, H.-J. *Prog. Surf. Sci.* **2001**, *67*, 99.
- (15) Benedetti, S.; Benia, H. M.; Nilius, N.; Valeri, S.; Freund, H.-J. *Chem. Phys. Lett.* **2006**, *430*, 330.
- (16) Wollschläger, J.; Erdos, D.; Goldbach, H.; Hopken, R.; Schröder, K. M. *Thin Sol. Films* **2001**, *400*, 1.
- (17) Benedetti, S.; Torelli, P.; Luches, P.; Valeri, S.; Benia, H. M.; Nilius, N.; Renaud, G. *Phys. Rev. B* **2008**, *78*, 195411.
- (18) Benia, H. M.; Nilius, N.; Freund, H.-J. *Surf. Sci. Lett.* **2007**, *601*, L55. Benia, H. M.; Myrach, P.; Nilius, N. *New J. Phys.* **2008**, *10*, 013010.
- (19) Sterrer, M.; Heyde, M.; Nowicki, M.; Nilius, N.; Risse, T.; Rust, H.-P.; Pacchioni, G.; Freund, H.-J. *J. Phys. Chem. B* **2006**, *110*, 46.
- (20) Benia, H. M.; Lin, X.; Gao, H. J.; Nilius, N.; Freund, H.-J. *J. Phys. Chem. C* **2007**, *111*, 10528.
- (21) Mg particle formation is observed only beyond 1 ML metal exposure. The first atoms are apparently integrated into the MgO film, for example, by attaching to O-rich step edges in the surface. The Mg incorporation might be facilitated by the availability of O<sub>2</sub> from the rest gas or Mo support.
- (22) Zhu, J.; Farmer, J. A.; Ruzycski, N.; Xu, L.; Campbell, C. T.; Henkelman, G. *J. Am. Chem. Soc.* **2008**, *130*, 2314.
- (23) Sterrer, M.; Risse, T.; Heyde, M.; Rust, H.-P.; Freund, H.-J. *Phys. Rev. Lett.* **2007**, *98*, 206103.
- (24) Pacchioni, G.; Giordano, L.; Baistrocchi, M. *Phys. Rev. Lett.* **2005**, *94*, 226104.
- (25) Yudanov, I.; Pacchioni, G.; Neyman, K.; Rosch, N. *J. Phys. Chem. B* **1997**, *101*, 2786. Del Vitto, A.; Pacchioni, G.; Delbecq, F. O.; Sautet, P. *J. Phys. Chem. B* **2005**, *109*, 8040.
- (26) Xu, L.; Henkelman, G. *Phys. Rev. B* **2008**, *77*, 205404.
- (27) Palik E. D. *Handbook of Optical Constants of Solids*; Academic: Orlando, FL, 1985.
- (28) Downes, A.; Welland, M. E. *Appl. Phys. Lett.* **1998**, *72*, 2671.
- (29) Johansson, P.; Monreal, R.; Apell, P. *Phys. Rev. B* **1990**, *42*, 9210. Anisimovas, E.; Johansson, P. *Phys. Rev. B* **1999**, *59*, 5126.
- (30) The two-step nature of electron transport through a single particle gives rise to Coulomb charging effects in the differential conductance, which were however not resolved at the high bias voltage used for optical excitations.
- (31) Chen J. C. *Introduction to Scanning Tunneling Microscopy*; Oxford University Press: New York, 1993.
- (32) Giordano, L.; Cinquini, F.; Pacchioni, G. *Phys. Rev. B* **2005**, *73*, 045414.
- (33) Gundlach, K. H. *Sol. Stat. Electron* **1966**, *9*, 949.
- (34) Binnig, G.; Frank, K. H.; Fuchs, H.; Garcia, N.; Reihl, B.; Rohrer, H.; Salvan, F.; Williams, A. R. *Phys. Rev. Lett.* **1985**, *55*, 991.
- (35) Kolesnychenko, O. Y.; Kolesnichenko, Y. A.; Shklyarevskii, O. I.; van Kempen, H. *Physica B* **2000**, *291*, 246.